Dyes and Pigments 219 (2023) 111641

Contents lists available at ScienceDirect

Dyes and Pigments

journal homepage: www.elsevier.com/locate/dyepig

Biotin-modified cyclometalated iridium-based photosensitizers as mitochondria-targeted theranostic agents for tumor photodynamic therapy *in vitro* and *in vivo*

Lai Wei [a], Xiangdong He [a], Xinyue Shang [a], Martha Kandawa-Shultz [c], Guoqiang Shao [b,**], Yihong Wang [a,*]

[a] School of Chemistry and Chemical Engineering, Southeast University, Nanjing, 211189, China
[b] Department of Nuclear Medicine, Nanjing First Hospital, Nanjing Medical University, Nanjing, 211166, China
[c] Department of Chemistry and Biochemistry, University of Namibia, Windhoek, 13301, Namibia

ARTICLE INFO

Keywords:
Biotin
Ir(III) complex
Mitochondria targeting
Photodynamic therapy
Apoptosis

ABSTRACT

Photodynamic therapy (PDT) is a promising non-invasive treatment technique for various types of cancer. Photoluminescent cyclometalated Ir(III) complexes, a distinctive genre of photosensitizers (PSS), have garnered significant interest due to their exceptional selective toxicity towards cancerous cells and minimal cytotoxicity towards normal cells. This study aimed to investigate the application of three newly designed biotin-modified cyclometalated Ir(III) complexes (**Ir1**-**Ir3**) for the treatment of cancer. The three complexes were found to have good photocatalytic activity, with singlet oxygen ($^1O_2$) yields ranging from 0.24 to 0.65 in aqueous solutions. The results suggest that these complexes have the potential as phototherapeutic and photodiagnostic agents for cancer treatment. Additionally, the biotin fragments in the **Ir1**-**Ir3** structures enable their selective targeting of tumor cells. Notably, **Ir3** displayed negligible dark toxicity towards A549 human lung cancer cells (IC_{50} > 100 μM), but its value decreased to 0.25 μM after 15 min of 425 nm (40 mW/cm^2) light exposure. Furthermore, these complexes exhibited low phototoxicity towards non-cancerous BHK mouse kidney cells. Further investigation demonstrated that **Ir3** had potent targeting abilities for mitochondria, and could trigger cell apoptosis through the activation of ROS-mediated mitochondrial signaling pathways under 425 nm light irradiation. *In vivo* studies revealed that **Ir3** effectively suppressed tumor growth in A549 xenograft-bearing mice when exposed to 425 nm light. These results indicate that **Ir3** has the potential to be a valuable photosensitizer drug for the photodynamic treatment of tumors.

1. Introduction

In recent years, research on cancer treatment has been one of the hotspots in the field of life sciences [1,2]. Safer and more effective cancer treatment methods are needed due to the various side effects and limitations of traditional treatments such as surgery, chemotherapy, and radiation therapy [3]. Photodynamic therapy (PDT) is a non-invasive treatment method that shows promise in treating a range of diseases, such as cancer, skin diseases, ophthalmic diseases, and oral diseases. Its therapeutic effects have been increasingly recognized, making it a valuable treatment option [4–9]. This therapy mainly relies on three non-toxic components: photosensitizers, light of appropriate wavelengths and molecular oxygen ($^3O_2$). The synergistic action of these three harmless components can produce reactive oxygen species (ROS), which can disrupt the regular function of cancer cells and lead to apoptosis [10,11]. In the process of PDT treatment for tumors, the least dose of toxic photosensitizer is first administered to the patient's body. Then, the tumor site is irradiated with light, causing the photosensitizer and light to combine and produce reactive oxygen, which damages cellular functions and ultimately leads to cell death. It's important to note that the photodynamic effect is limited to the irradiated area due to the low diffusion rate and short lifespan of reactive oxygen species [12–14]. Compared to traditional cancer treatment methods such as chemotherapy, radiation therapy, and surgery, PDT has several

* Corresponding author.
** Corresponding author.
E-mail addresses: guoqiangshao@163.com (G. Shao), yihongwang@seu.edu.cn (Y. Wang).

https://doi.org/10.1016/j.dyepig.2023.111641
Received 6 May 2023; Received in revised form 24 July 2023; Accepted 21 August 2023
Available online 22 August 2023

significant advantages, including non-invasiveness, local treatment, repeatability, tissue selectivity, no toxic side effects and no adverse effects or discomfort to patients [15]. Currently, PDT has become a mature treatment method and has been widely applied in clinical medicine, biomedical research and the field of life sciences [16].

Platinum-based chemotherapy drugs, such as cisplatin, carboplatin, oxaliplatin, nedaplatin and lobaplatin, have been extensively utilized in cancer treatment. Nevertheless, these drugs have vast drawbacks, including toxic side effects, drug resistance, high cost, and negative impact on patients' quality of life. For these reasons, the scientific community turned its attention to explore other metal-based medicines [17]. Over the past few years, iridium-based complexes have emerged as attractive alternatives to platinum-based drugs due to their better properties [18–21]. Recent research has shown that cyclometalated Ir (III) complexes have excellent photo-physical properties and remarkable anti-cancer activity. Compared to platinum complexes, cyclometalated Ir(III) complexes have better ligand substitution kinetics and more diverse molecular structures, which results in better treatment outcomes for tumors [10,22,23]. Additionally, these complexes also exhibit several advantages, such as long fluorescence lifetimes (~ms), good chemical stability, high quantum yield, efficient charge transfer ability, tunable optical and chemical properties, strong photobleaching resistance, excellent cell permeability, and the ability to generate ROS through their interaction with molecules inside the cells in the tumor [10,24,25]. Given the remarkable photophysical and photochemical properties of Ir(III) complexes, they can be utilized to design diverse, highly sensitive fluorescent probes for tumor imaging and diagnosis [26,27]. In recent years, there has been a growing interest among researchers in modifying the properties of cyclometalated Ir(III) complexes through the design of suitable ligands and structural modifications. These efforts aim to improve the performance of these complexes and broaden their potential applications [28–30].

The majority of drugs used for tumor treatment cannot specifically target tumors, and typically only a small portion of these drugs can effectively act on the affected area after entering the body. This is the fundamental reason for the low efficacy of these drugs and the occurrence of adverse drug reactions [31,32]. Biotin, also known as vitamin H or coenzyme R, is a water-soluble vitamin that is essential for the synthesis of vitamin C and for the normal metabolism of fats and proteins. Biotin is usually transported in mammalian cells via a Na^+-dependent multivitamin transporter (SMVT). To meet the demands of rapid growth, certain types of cancer cells overexpress SMVT [33]. Recently, it has been reported that strategies utilizing the overexpression of biotin receptors in cancer cells and the modification of drugs with biotin fragments have been applied in various fields, including bioimaging, cancer therapy, and biosensing [16,33–36]. Biotin-conjugated drugs utilize the highly specific binding between biotin and biotin receptors to accurately deliver drugs to tumor cells, achieving selective killing of tumor cells. Biotin-conjugated drugs have many advantages in tumor treatment. Firstly, they can achieve targeted delivery of drugs, reduce toxicity to normal cells, and minimize adverse reactions. Secondly, by designing and synthesizing different drug molecules containing biotin structures, diversification and personalization can be achieved, thereby improving the therapeutic effect [33,34,37].

Mitochondria are responsible for producing ATP in most cells and play a significant role in tumor development and progression. When tumor cells are exposed to hypoxic conditions, it affects their mitochondrial metabolism, making them more sensitive to oxidative stress or reactive species [38]. Therefore, mitochondria represent an appropriate subcellular target for PDT [39].

In this study, we designed and prepared three biotinylated Ir(III) complexes (**Ir1**-**Ir3**) for tumor-targeted imaging and therapy (Scheme 1). Under 425 nm (40 mW/cm^2) light irradiation, **Ir1**-**Ir3** exhibited remarkable anti-tumor effects against various tumor cells in vitro, with relatively low toxicity toward normal cells. The antitumor mechanism of **Ir3** was elucidated, including subcellular localization, mitochondrial dysfunction, ROS production and cell apoptosis. Moreover, *in vivo* biological evaluation of **Ir3** was conducted in A549 xenograft-bearing mice, demonstrating significant antitumor effects in the **Ir3**-treated group of mice exposed to 425 nm (40 mW/cm^2) light irradiation (Scheme 1).

2. Results and discussion

2.1. Ir(III) complexes synthesis and photophysical characterization

The synthetic route of the ligands and Ir(III) complexes **Ir1**-**Ir3** and **Ir3-NB** was displayed in Scheme 1 and Scheme S1. Their structures were confirmed by elemental analysis, ESI-MS, and ^{1}H NMR (Figs. S1–S14). The normalized UV–Vis absorption spectra of **Ir1**-**Ir3** in CH_2Cl_2, CH_3OH and H_2O were shown in Fig. S15. The relatively intense absorption bands below 350 nm were ascribed to the $\pi\rightarrow\pi^*$ transitions, while the relatively intense absorption bands to 500 nm could be assigned to the

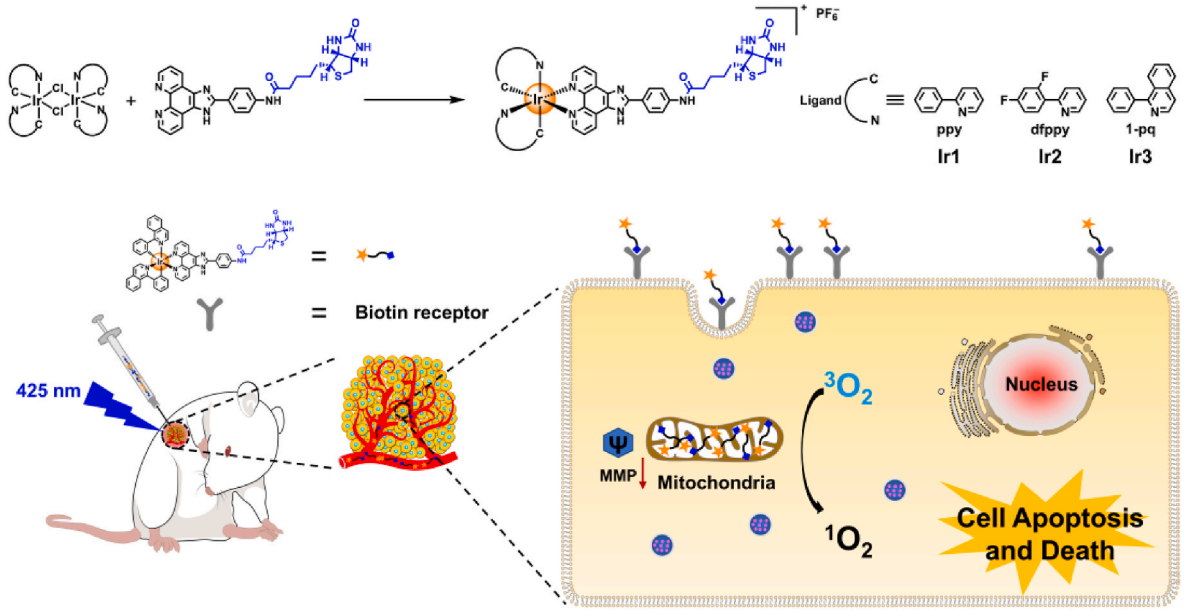

Scheme 1. Schematic of the preparation process of **Ir1**-**Ir3** and photodynamic antitumor mechanism of **Ir3**.

metal-to-ligand charge transfer (MLCT) and ligand-to-ligand charge transfer (LLCT) characters. Upon excitation at 425 nm, the fluorescence emission spectra from 450 to 750 nm and the normalized fluorescence emission spectra from 500 to 750 nm of **Ir1**-**Ir3** in CH_2Cl_2, CH_3OH and H_2O were presented in Fig. S16. Upon excitation at 425 nm, the Ir(III) complexes (**Ir1**-**Ir3**) exhibited a color change from green to red in these solvents. Additionally, all complexes had large Stokes shifts, with **Ir3** having the largest shift, followed by **Ir1** and **Ir2**. The normalized fluorescence spectra revealed that Ir1-Ir3 exhibited two fluorescence emission peaks. As the solvent polarity increased, the fluorescence intensity of the three iridium complexes decreased, and the peak shifted towards longer wavelengths (redshifted). This phenomenon can be attributed to the alteration in the local environment of the molecules caused by the increase in solvent polarity, leading to changes in fluorescence intensity and wavelength displacement.

2.2. Singlet oxygen ($^1O_2$) generation rate

To assess the potential of **Ir1**-**Ir3** as photosensitizers against cancer cells via photodynamic therapy (PDT), it is crucial to evaluate their capacity to generate reactive oxygen species (ROS), with a particular focus on singlet oxygen ($^1O_2$) generation [40]. The quantum yields (Φ_Δ) of $^1O_2$ produced from **Ir1**-**Ir3** were determined in H_2O, utilizing [Ru(bpy)$_3$]Cl$_2$ as a standard, by monitoring the changes in the UV–vis spectra of 9,10-Anthracenediyl-bis(methylene)dimalonic Acid (ABDA) at 380 nm. While the mixture solution of **Ir1**-**Ir3** and ABDA was irradiated (425 nm, 40 mW/cm^2), a remarkably decreased absorbance occurred. The Φ_Δ values of **Ir1**-**Ir3** and standard were determined as the following order: **Ir2** (0.65) > **Ir1** (0.37) > **Ir3** (0.24) > [Ru(bpy)$_3$]Cl$_2$ (0.18) (Fig. 1 and Fig. S17). These results indicate that **Ir1**-**Ir3** can produce $^1O_2$ when exposed to light irradiation, making them a promising option for PDT applications.

2.3. Time-dependent density functional theory (TD-DFT) calculations

Time-dependent density functional theory (TD-DFT) calculations were employed to further explain the generation mechanism of ROS of **Ir1**-**Ir3**. As shown in Fig. 2A and Table S1, the lowest unoccupied molecular orbital (LUMO) part of **Ir1**-**Ir3** was primarily concentrated on the ligand containing biotin fragment, while the highest occupied molecular orbital (HOMO) predominantly resided on the cyclometalated ligands for **Ir1** and **Ir3** and the ligand containing biotin fragment for **Ir2**. In contrast to **Ir1** (ΔE_g = 3.33 eV) and **Ir3** (ΔE_g = 3.14 eV), **Ir2** (ΔE_g = 3.46 eV) exhibited a distinct separation in the HOMO and LUMO distributions. Additionally, we conducted further calculations to determine the singlet and triplet energy levels of **Ir1**-**Ir3** (Fig. 2B and Table S1). The energy gap $\Delta E_{(S1\text{-}T1)}$ between the S1 and T1 states was measured to be 0.11 eV for **Ir1**, 0.76 eV for **Ir2** and 0.44 eV for **Ir3**. Crossing from the lowest singlet excited state (S1) to the nearest triplet excited state (T1) within PSs after being stimulated by light, the excited electrons combine with triplet oxygen ($^3O_2$) to generate singlet oxygen ($^1O_2$), which is highly toxic to tumor cells. So the singlet oxygen ($^1O_2$) generation capacity in the whole process mainly depends on the ability of photosensitizer to intersystem crossing (ISC). The lower energy gap in **Ir1**-**Ir3** facilitated the singlet-triplet intersystem crossing (ISC) process. Apparently, **Ir1**-**Ir3** all show smaller $\Delta E_{(S1\text{-}T1)}$ values, leading to an effective $^1O_2$ generation. Furthermore, the calculated results revealed a significant difference in the excited state energy between **Ir2** and **Ir1** as well as **Ir3**. Notably, the fluorescence signal of **Ir2** was barely detectable beyond 450 nm, which aligns with the experimental findings indicating that **Ir2** exhibited the weakest fluorescence (Table S1).

2.4. Lipophilicity

To determine the hydrophilicity and lipophilicity of **Ir1**-**Ir3**, the n-octanol/water partition coefficient of **Ir1**-**Ir3** were determined using the shake-flask method. As shown in Fig. S18, the lipophilicity indices of the three complexes followed the order of **Ir3** > **Ir2** > **Ir1**. It is important to note that the lipophilicity of a drug can significantly influence the rate and mechanism of drug molecules traversing the cell membrane. Generally, drugs with higher lipophilicity have an enhanced ability to penetrate the lipid bilayer cell membrane and gain access to the interior of the cell. **Ir3** has higher lipophilicity and therefore may be better taken up by cells.

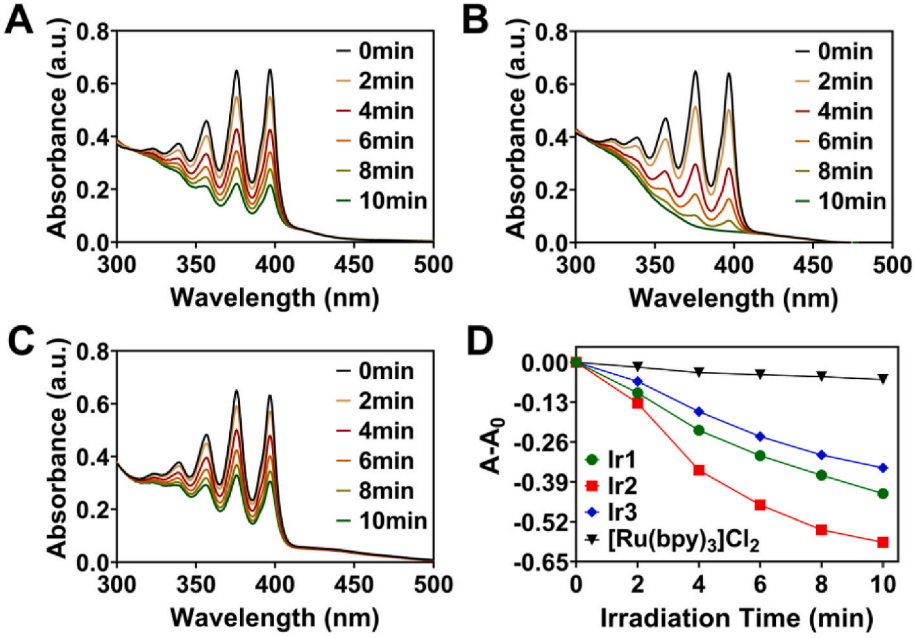

Fig. 1. The absorbance of ABDA (100 μM) after photodecomposition under visible light irradiation (425 nm, 40 mW/cm^2) over different times in the case of (A) **Ir1**, (B) **Ir2** and (C) **Ir3** in H_2O solution (20 μM). (D) The absorbance changes of ABDA at 380 nm with **Ir1**, **Ir2**, **Ir3** and [Ru(bpy)$_3$]Cl$_2$ in H_2O solution (20 μM) under visible light irradiation (425 nm, 40 mW/cm^2) over different times.

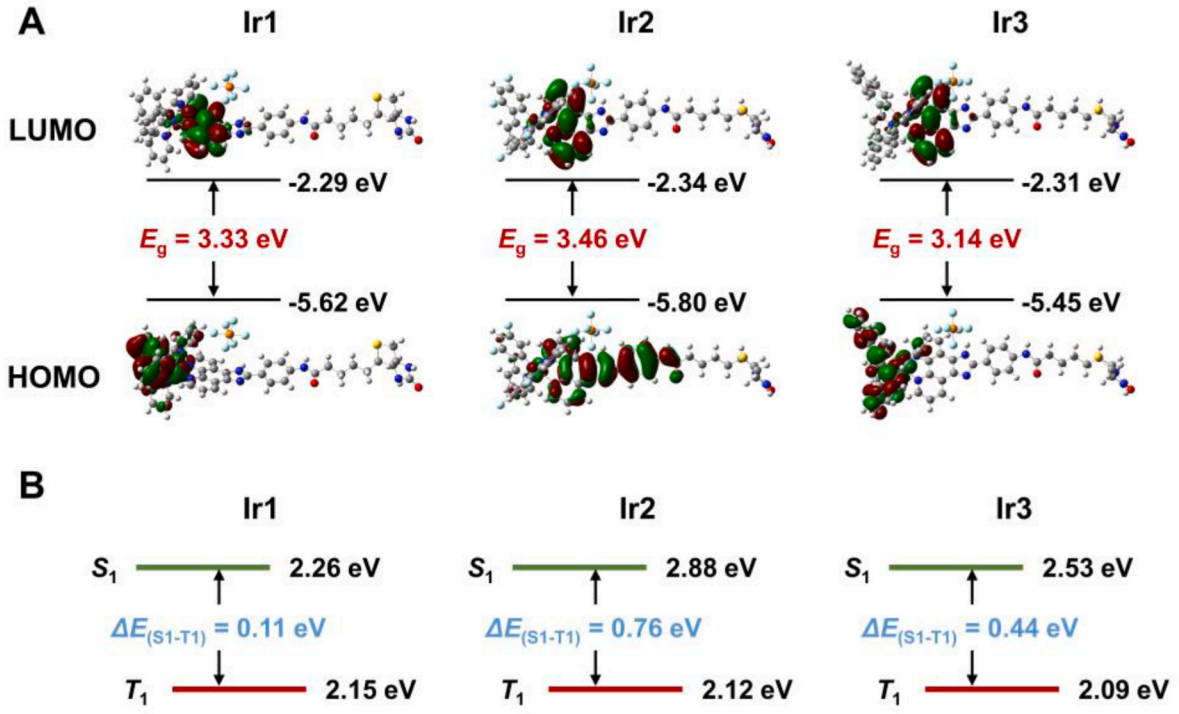

Fig. 2. (A) HOMO–LUMO distribution at S_1 for **Ir1**-**Ir3**. (B) The energy gap between S_1 and T_1 for **Ir1**-**Ir3** from TD-DFT (Gaussian/B3LYP/6-311G(d)).

2.5. Cellular uptake

To establish the functional significance of the biotin moiety in facilitating the localization of the **Ir1**-**Ir3** to biotin receptor-enriched tumor cells, we conducted an incubation experiment in which the **Ir1**-**Ir3** were exposed to human lung cancer cells (A549) and mouse kidney cells (BHK) for 3 h. A549 and BHK cells, as biotin-positive and negative cell systems, respectively [41]. Flow cytometry was utilized to analyze the internalization of cells and quantify the uptake of **Ir1**-**Ir3**. As shown in Fig. 3A–F, A549 cells treated with **Ir1**-**Ir3** exhibited strong fluorescence signals compared to control cells, approximately 13.2-fold for **Ir1**, 11.6-fold for **Ir2**, and 49.8-fold for **Ir3**. In contrast, negligible fluorescence was observed in BHK cells. These findings suggest that the amplified uptake of **Ir1**-**Ir3** in A549 cells is primarily attributed to receptor-mediated endocytosis through the biotin receptors, which is facilitated by the interaction between the biotin moiety and the biotin receptor on the surface of tumor cells.

Considering the favorable performance of **Ir3**, further experiments were conducted to determine the cellular uptake of this complex. The confocal laser scanning microscope (CLSM) images showed no significant fluorescence signal in the normal cell group (BHK) after 3 h of **Ir3** treatment (Fig. 3G). In contrast, the fluorescence intensity of **Ir3** in A549 cells increased significantly with the incubation time (Fig. 3H). The results of the flow cytometry showed that compared with the control group, the fluorescence signal of A549 cells increased significantly after incubation with **Ir3** for different times (15.1-fold for 1h, 30.4-fold for 2h and 49.2-fold for 3h, Fig. 3I and K). On the contrary, only negligible fluorescence was observed in BHK cells even after 3 h of incubation with **Ir3** (6-fold, Fig. 3J and K). These results further demonstrate that the biotin-modified complex **Ir3** promotes the uptake and selective accumulation of **Ir3** by overexpressing the biotin receptor in cancer cells (A549) through receptor-mediated endocytosis. At the same time, the higher lipophilicity of **Ir3** also promotes its uptake by cells. The effective uptake of the photosensitizer by cells may potentially improve PDT.

2.6. In vitro cytotoxicity and photocytotoxicity

To evaluate the impact of illumination time on the sensitivity of **Ir3**-treated A549 cells, the viability of these cells was assessed via the MTT assay across a range of illumination times (0 min, 5 min, 10 min,15 min and 20 min). As shown in Fig. S19, when the concentration of **Ir3** was constant, the viability of A549 cells decreased with increasing illumination time (0 min, 5 min, 10 min, and 15 min, 425 nm, 40 mW/cm^2). However, a negligible decline in cell viability was observed for illumination times exceeding 15 min (15 min, 20 min). Hence, 15 min was chosen as the illumination time of PDT in this study.

The cytotoxic effect and PDT activities of **Ir1**-**Ir3** and cisplatin in A549, MDA-MB-231, MCF-7 and BHK cells were determined by MTT assay (Table 1). Under 425 nm, 40 mW/cm^2 light irradiation for 15min, all three Ir(III) complexes-treated cancer cells exhibited high phototoxicity. The cytotoxic effect of **Ir1**-**Ir3** under dark conditions was negligible with $IC_{50} > 100$ μM. Notably, **Ir3** showed the highest phototoxicity index (PI) > 416 in A549 cells. In addition, **Ir1**-**Ir3** exhibited relatively low phototoxic effects in non-cancerous cells (BHK cells), which may be attributed to the low expression of biotin receptors that mediate cellular uptake of **Ir1**-**Ir3** in non-cancerous cells (BHK cells). However, it should be noted that the phototoxicity index (PI) of **Ir1**-**Ir3** in non-cancerous cells (BHK cells), although much smaller compared to cancer cells, reached values of **Ir1** > 13.3, **Ir2** > 16.4, and **Ir3** > 17.9, indicating that the overexpression of biotin receptors in cancer cells is a primary pathway for **Ir1**-**Ir3** uptake, a passive uptake mechanism cannot be completely ruled out.

Inspired by the above results, Ir(III) complex without biotin group modification was synthesized (**Ir3-NB**) and further investigated for its anticancer activity by MTT assay. As shown in Tables 1 and **Ir3-NB** was more phototoxic to the selected cell lines than **Ir1**-**Ir3**, but **Ir3-NB** also showed high toxicity to the selected cancer cell lines and non-cancer cell lines under dark conditions. These results indicated that the selective phototoxicity of **Ir1**-**Ir3** to tumor cells was enhanced by the modification of biotin groups.

Notably, the photocytotoxicity of **Ir1**-**Ir3** was significantly

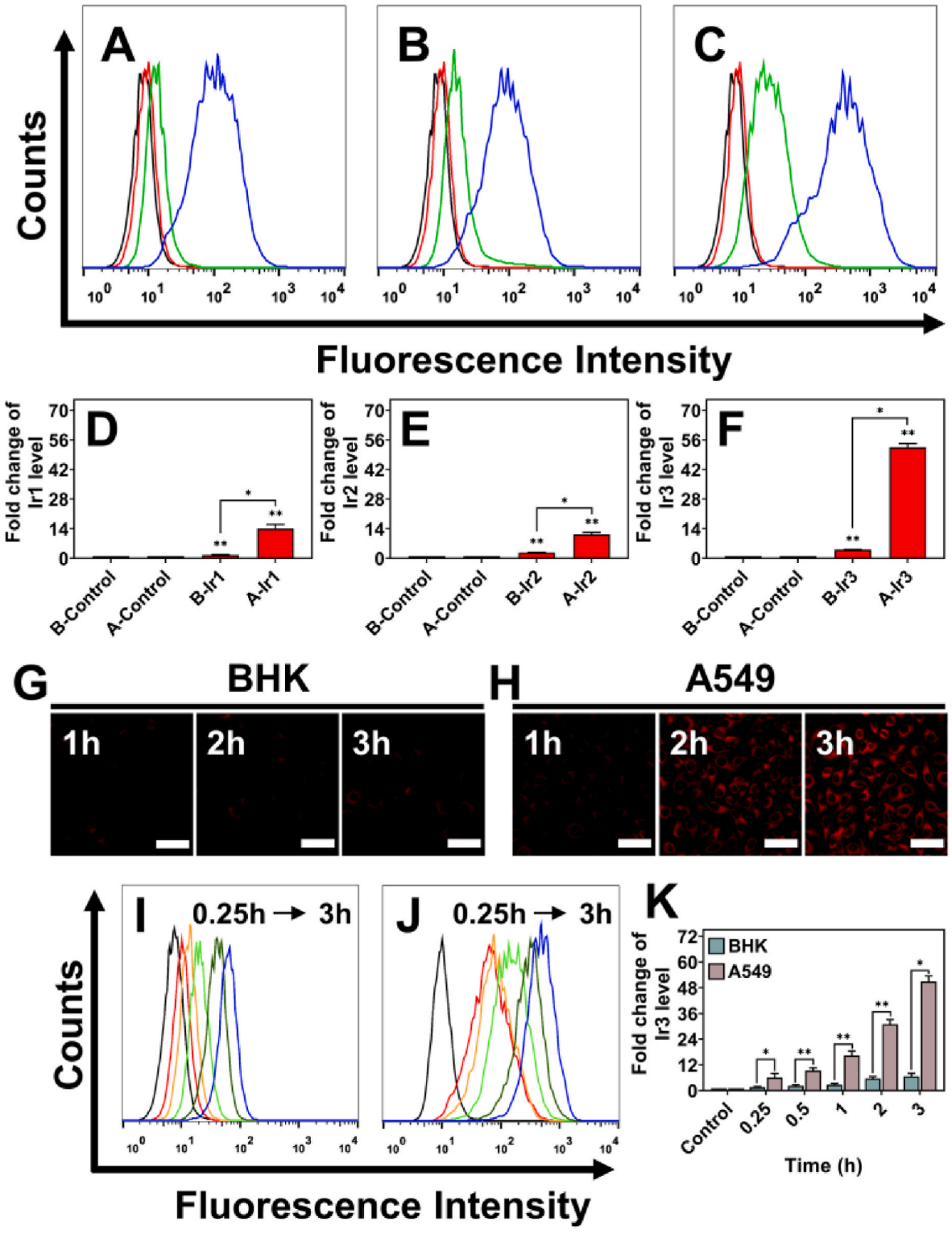

Fig. 3. Flow cytometry analysis of BHK and A549 cells treated with (A, D) **Ir1** (10 μM), (B, E) **Ir2** (10 μM), and (C, F) **Ir3** (10 μM) for 3 h. BHK cells treated with the complexes: green lines, A549 cells treated with the complexes: blue lines, untreated BHK cells: black lines, and untreated A549 cells: red lines. B means BHK cells, and A means A549 cells. Confocal microscopy images of BHK (G) and A549 (H) cells treated with **Ir3** (10 μM) for 1, 2, and 3 h. The samples were excited at 400 nm and detected at 590 ± 20 nm. Scale bar = 20 μm. Flow cytometry analysis of BHK (I, K) and A549 (J, K) cells treated with **Ir3** (10 μM) for 0.25, 0.5, 1, 2, and 3h. Data are represented as mean ± standard deviation. The single asterisk symbol (*) represents $p < 0.05$, and the double asterisk symbol (**) represents $p < 0.01$.

irrelevant to the quantum yield of $^1O_2$ formation, implying that the photokinetic activity of these complexes may be influenced by the level of cellular uptake, $^1O_2$ production capacity and target binding affinity. In addition, **Ir3** was more effective against tumor cells under 425 nm (40 mW/cm^2) light irradiation. Therefore, **Ir3** was selected as a targeting compound to elucidate the mechanism of its anticancer effect.

Table 1
IC_{50} Values (μM) and Photocytotoxicity Indices (PI) for **Ir1**-**Ir3** and **Ir3-NB** from an MTT assay.

	IC_{50} (μM)							
	A549		MDA-MB-231		MCF-7		BHK	
Complex	Dark[a] (Light[b])	PI[c]	Dark[a] (Light[b])	PI[c]	Dark[a] (Light[b])	PI[c]	Dark[a] (Light[b])	PI[c]
Ir1	> 100 (1.21 ± 0.08)	> 82.6	> 100 (1.09 ± 0.12)	> 91.7	> 100 (1.58 ± 0.11)	> 63.3	> 100 (7.50 ± 0.21)	> 13.3
Ir2	> 100 (1.35 ± 0.11)	> 74.1	> 100 (1.07 ± 0.15)	> 93.5	> 100 (1.15 ± 0.14)	> 87.0	> 100 (6.11 ± 0.06)	> 16.4
Ir3	> 100 (0.24 ± 0.02)	> 416.7	> 100 (0.38 ± 0.06)	> 263.2	> 100 (0.51 ± 0.03)	> 196.1	> 100 (5.60 ± 0.09)	> 17.9
Ir3-NB	7.84 ± 0.12 (0.13 ± 0.01)	60.3	8.18 ± 0.23 (0.16 ± 0.03)	51.1	9.29 ± 0.14 (0.18 ± 0.02)	51.6	6.07 ± 0.11 (0.14 ± 0.05)	43.4
Cisplatin	25.30 ± 0.83 (24.70 ± 0.52)	1.0	13.43 ± 0.09 (13.02 ± 0.32)	1.0	18.73 ± 0.15 (17.96 ± 0.27)	1.0	36.20 ± 2.10 (34.10 ± 1.10)	1.0

[a] Cell lines were treated with **Ir1**-**Ir3 and Ir3-NB** for 24 h in the dark.
[b] Cell lines were treated with **Ir1**-**Ir3 and Ir3-NB** for 3 h in the dark, and then exposed to light irradiation at 425 nm (40 mW/cm^2) for 15 min.
[c] PI = Phototoxicity index, which represents the ratio of IC_{50} values in the absence and presence of light irradiation.

2.7. Cell cloning test

The growth inhibition of A549 cells by various concentrations of **Ir3** treatment was assessed using the colony formation assay. As shown in Fig. 4, under 425 nm (40 mW/cm^2, 15min) light conditions, colony formation of **Ir3**-treated A549 cells was dramatically reduced by increasing **Ir3** concentration. The colony formation rates were 69% at 0.125 μM, 24% at 0.25 μM and 2% at 0.5 μM, respectively. Conversely, the inhibitory effect of **Ir3** treatment on colony formation could be ignored in the dark, with a colony formation rate of 95% at 0.5 μM. This trend observed is consistent with that obtained from the MTT assay.

2.8. Subcellular location experiments

The intracellular localization of photosensitizers has a significant impact on the effectiveness of PDT [42]. Given that **Ir3** exhibits strong PDT activity in cancer cells, further investigations of its distribution within cells can be conducted through the confocal laser scanning microscope (CLSM). The images (Fig. 5) obtained from the confocal microscopy revealed that after 3 h of incubation with A549 in the dark, the Pearson co-localization coefficient between **Ir3** and the mitochondrial probe Mito-Tracker Green was 0.96, while under the same conditions, the Pearson co-localization coefficient between **Ir3** and the lysosomal probe Lyso-Tracker Green was 0.41. These results revealed that **Ir3** predominantly localized to the mitochondria, indicating that **Ir3** may induce cell death via the mitochondrial apoptosis pathway.

2.9. Mitochondrial damage

As presented above, **Ir3** is mainly localized in mitochondria, its effect on the membrane integrity of mitochondrial was assessed via 5,5′,6,6′-tetrachloro-1,1′,3,3′- tetraethyl benzimidazolylcarbocyanine iodide (JC-1) staining by flow cytometry. Mitochondrial depolarization can be revealed by a decrease in the ratio of red (JC-1 aggregates) to green (JC-1 monomers) fluorescence intensity [43]. As shown in Fig. 6 and Fig. S20, under 40 mW/cm^2, 425 nm light irradiation for 15min, the intensity ratio of red/green fluorescence in **Ir3**-treated A549 cells was reduced in a concentration-dependent manner. In contrast, the shift from red to green fluorescence was barely observed in **Ir3**-treated A549 cells under dark conditions. These results suggest that **Ir3** tends to impair the integrity of mitochondria in the light, but not in the dark.

2.10. ROS detection

Photodynamic therapy (PDT) relies on photosensitizers to generate cytotoxic reactive oxygen species (ROS), leading to tumor cell apoptosis [11]. Numerous studies have suggested that mitochondrial dysfunction is associated with excessive accumulation of ROS, which plays a decisive role in cell apoptosis [44]. 2′,7′-dichlorofluorescein diacetate (DCFH-DA) is a widely used ROS indicator. In the presence of ROS, DCFH reacts with ROS to form dichlorofluorescein (DCF), and the resulting fluorescence is proportional to ROS levels [45]. In this study, DCFH-DA was used as a fluorescent probe to detect the level of ROS in **Ir3**-treated A549 cells using confocal microscopy and flow cytometry. As shown in Fig. 7A and B, the fluorescence intensity of **Ir3**-treated A549 cells increased in a concentration-dependent manner with increasing **Ir3** concentration when irradiated with 425 nm (40 mW/cm^2, 15 min) light, indicating effective ROS production. In contrast, under dark conditions, negligible green fluorescence was observed in **Ir3**-treated A549 cells. Flow cytometry results (Fig. 7C and D) showed that under 425 nm light irradiation, the average DCF fluorescence intensity in **Ir3**-treated A549 cells increased 6.1-fold, 7.7-fold, and 10.2-fold for 0.125 μM, 0.25 μM, and 0.5 μM of **Ir3**, respectively. In contrast, there was almost no increase in the DCF average fluorescence intensity in **Ir3**-treated A549 cells under dark conditions.

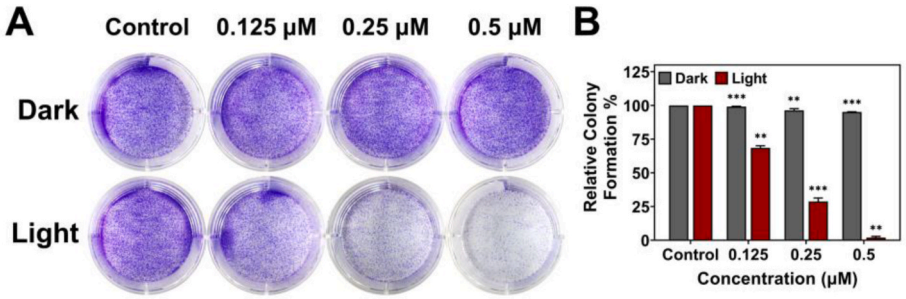

Fig. 4. (A) Colony formation of A549 cells at 10 days after treatment with **Ir3** (0.125 μM, 0.25 μM and 0.5 μM) in the dark and with light irradiation. (B) The quantification analysis of (A). Data are represented as mean ± standard deviation. The single asterisk symbol (*) represents $p < 0.05$, the double asterisk symbol (**) represents $p < 0.01$ and the triple asterisk symbol (***) represents $p < 0.001$.

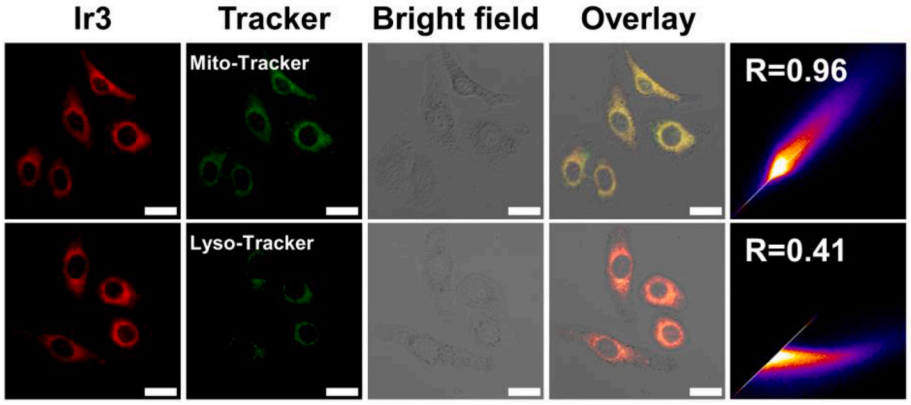

Fig. 5. CLSM co-localization images of **Ir3** (10 μM, 3 h) with Mito-Tracker Green (Mito-Tracker; 100 nM, 30 min) and Lyso-Tracker Green (Lyso-Tracker; 50 nM, 30 min) in A549 cells. $\lambda_{ex} = 500$ nm (Mito-Tracker and Lyso-Tracker) and 400 nm (**Ir3**); $\lambda_{em} = 510 \pm 10$ nm (Mito-Tracker and Lyso-Tracker) and 590 ± 20 nm (**Ir3**). All images share the same scale bar, 20 μm.

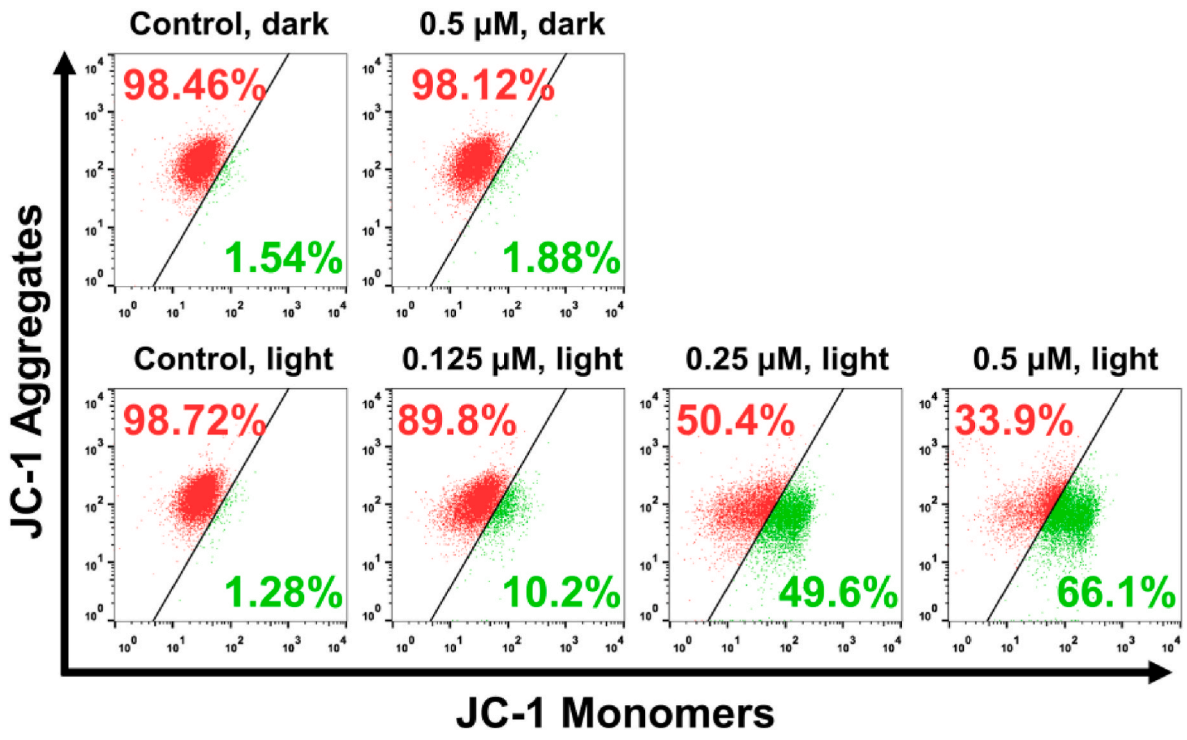

Fig. 6. Flow cytometry analysis of the effect of **Ir3** on the mitochondrial membrane potential of A549 cells ($\lambda_{ex} = 490$ nm and $\lambda_{em} = 530$ nm).

2.11. Apoptosis induction

To further validate the apoptotic pathway triggered by **Ir3**, we conducted experiments on A549 cells with different concentrations of **Ir3** treatments under both light and dark conditions. A double-staining technique using FITC-Annexin V/PI was utilized to label the A549 cells and the apoptotic rate was analyzed via flow cytometry. As shown in Fig. 8 and Fig. S21, the percentages of early and late apoptotic cells in A549 cells treated with **Ir3** increased in a concentration-dependent manner under 425 nm light conditions, indicating that apoptosis occurred in A549 cells. In contrast, under dark conditions, the percentages of early and late apoptotic cells in A549 cells treated with **Ir3** remained almost unchanged.

2.12. Inhibition of cell migration

The effect of **Ir3** on the horizontal migration of A549 cells was evaluated by wound healing assay. As shown in Fig. 9, cells were treated with different concentrations of **Ir3** for 12 and 24 h in the dark or under the indicated light conditions. Notably, cells treated with 0.125, 0.25, and 0.5 μM of **Ir3** under 425 nm (40 mW/cm^2, 15 min) light exhibited significant time-dependent inhibition of wound healing integrity compared to cells in the dark. The results indicate that **Ir3** may exert an important role in inhibiting the wound-healing process under light irradiation conditions.

2.13. In vivo antitumor evaluation

The in vitro experimental findings demonstrate that **Ir3** specifically targets biotin receptors that are overexpressed in tumor cells and localizes in mitochondria, exhibiting effective efficacy in photodynamic therapy (PDT). To further investigate the therapeutic effects of **Ir3**, an *in vivo* experiment was conducted using A549 nude mouse xenograft models (Fig. 10A). Tumor-bearing mice were randomly divided into four

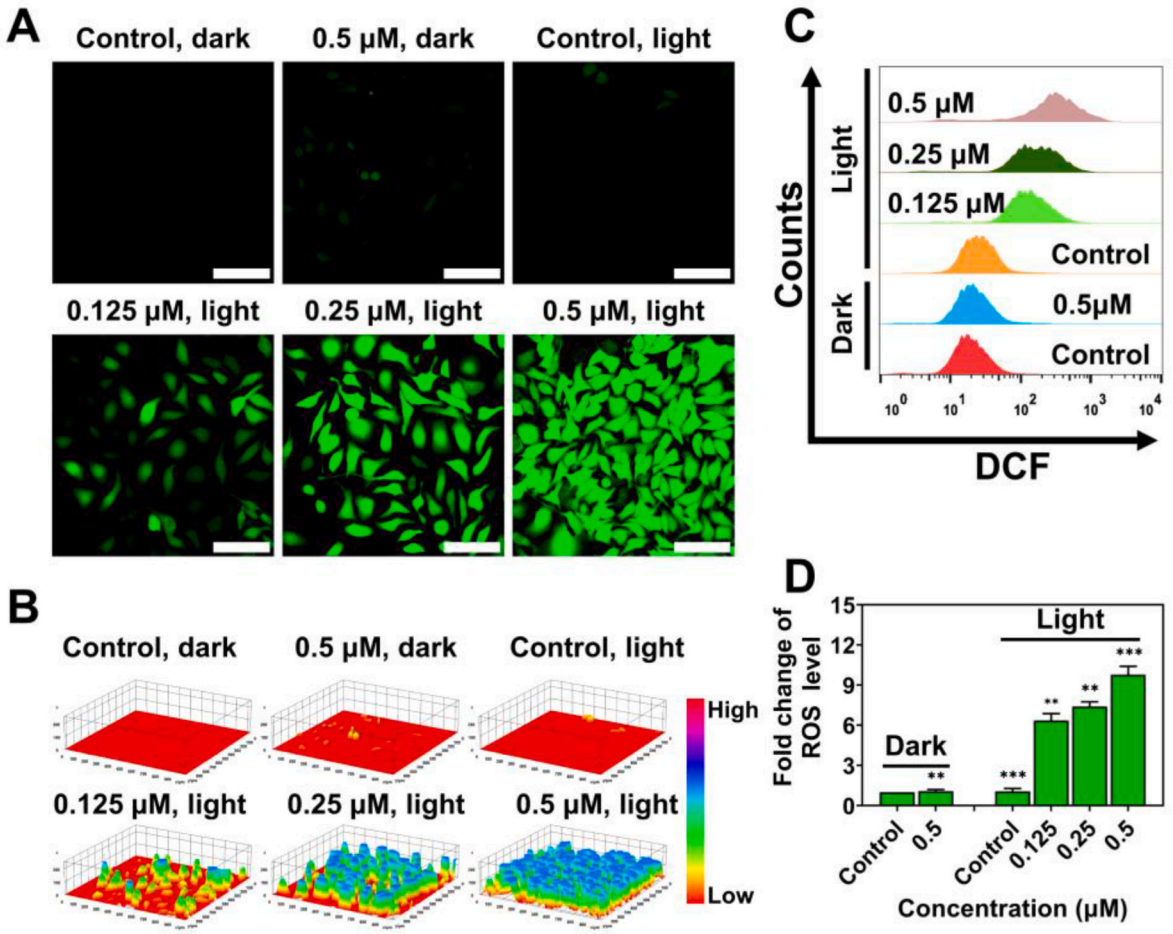

Fig. 7. (A) Confocal microscopy images of ROS generation in different concentrations of **Ir3** (3 h)-treated A549 cells and DCF (10 μM, 0.5 h, $\lambda_{ex} = 488$ nm, $\lambda_{em} = 530$ nm) before and after light irradiation. Scale bar = 20 μm. (B) The 3D image of (A). (C) Flow cytometry of ROS generation in different concentrations of **Ir3** (3 h)-treated A549 cells. (D) The quantification analysis of (C). Data are represented as mean ± standard deviation. The double asterisk symbol (**) represents $p < 0.01$ and the triple asterisk symbol (***) represents $p < 0.001$.

groups, each containing four mice: the saline dark group, saline light group, **Ir3** dark group, and **Ir3** light group. Mice in the **Ir3** dark and **Ir3** light groups were intratumorally injected with **Ir3** at a dose of 10 mg/kg. Subsequently, the tumor site of mice in the **Ir3** light group was irradiated with 425 nm at 40 mW/cm^2 for 15 min, 3 h after injection. The saline dark group and the saline light group were treated with an equivalent dose of saline and light intensity. The body weight and tumor volume variation were recorded every three days to evaluate the therapeutic effect. The growth of tumors in the **Ir3** light group was remarkably inhibited, and the tumor volume significantly decreased over time. In stark contrast, the tumor volume in the other three groups increased sharply during the same period (Fig. 10B). After 21 days, there was no significant change in the weight of mice in all groups (Fig. 10C), demonstrating the biological safety of **Ir3**. After sacrificing the mice on day 21, tumor tissues were collected, photographed, and weighed. The tumor volume reduction was visually observed in the **Ir3** light group (Fig. 10E), and the tumor weight in the **Ir3** light group was significantly smaller than that in the other three groups (Fig. 10D). The tumor and normal organs (heart, liver, spleen, lung, and kidney) were subjected to histopathological analysis. Hematoxylin and eosin (H&E) staining of the tumor and normal organs showed that the structure of the tumor in the **Ir3** light group was severely damaged, with deformed nuclei, intercellular edema, and overall tumor tissue atrophy. The structure of the tumor in the **Ir3** dark group was slightly damaged, with a slight decrease in cell density. In the other control groups, the tumor cells were densely arranged, and no significant pathological abnormalities or inflammatory lesions, cell death, or apoptosis were observed in the normal organs (Fig. 10F). In summary, these results demonstrate that **Ir3** induces tumor cell death through PDT *in vivo*, and at the tested dose, it has no severe adverse effects on normal organs, making it an effective photosensitizer for tumor photodynamic therapy.

3. Conclusions

In summary, three novel Ir(III) complexes (**Ir1**-**Ir3**) incorporating biotin fragments were designed, synthesized, characterized, and evaluates their potential as photocatalysts for cancer therapy. These complexes showed strong phototoxicity against the tested human cancer cell lines with low phototoxicity toward normal mouse cells. Cell confocal imaging revealed that **Ir3** was preferentially taken up by A549 cancer cells through highly expressed biotin receptors and selectively targeted mitochondria. **Ir3** severely disrupted the physiological function of mitochondria, as evidenced by a decrease in mitochondrial membrane potential and an increase in ROS production and further led to apoptosis under 425 nm (40 mW/cm^2) light irradiation. The *in vivo* therapy results indicated that **Ir3** significantly inhibited the growth of A549 tumors in a mouse xenograft model under the light. From this viewpoint, the biotin-modified Ir(III) complex, **Ir3**, could be a promising candidate for molecular targeted photodynamic therapy (PDT). This study also highlights the potential of using this design strategy to develop multifunctional anticancer drugs with reduced side effects.

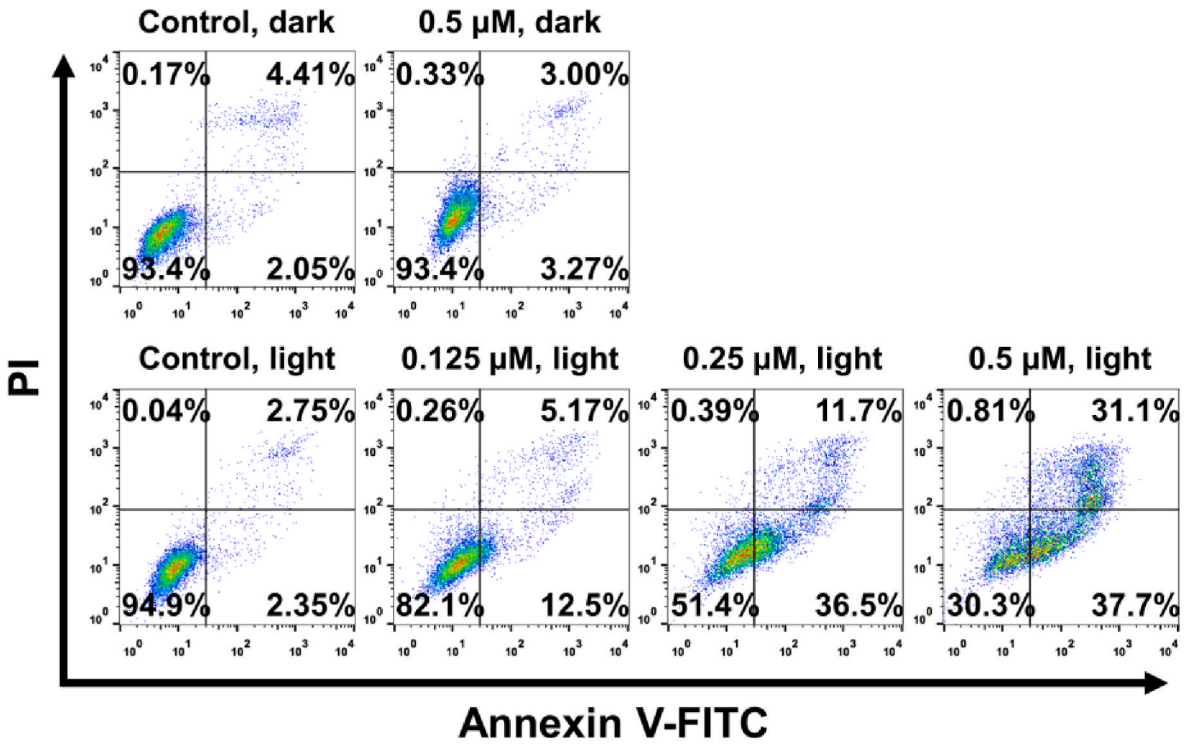

Fig. 8. Flow-cytometric quantification of double Annexin V/PI-labeled A549 cells treated with different concentrations of **Ir3** in the dark and under light (425 nm, 40 mW/cm^2).

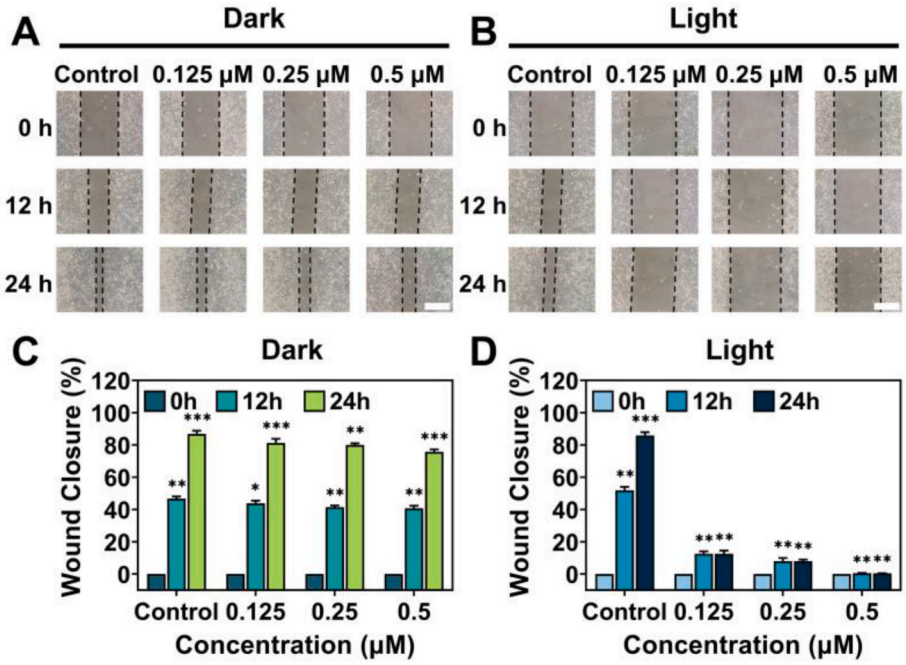

Fig. 9. The wound healing assay was carried out on **Ir3**-treated A549 cells. (A) The cells were treated with 0.125, 0.25, and 0.5 μM of **Ir3** for 0, 12 and 24 h in the dark. (B) The cells were treated with 0.125, 0.25, and 0.5 μM of **Ir3** for 0, 12 and 24 h under 15 min of light irradiation at 425 nm. Scale bars, 200 μm. The results of wound healing assay for (C) dark and (D) light irradiation conditions. Wound closure (%) = [1 - (distance at indicated time)/(distance at 0 h)] × 100%. Data are represented as mean ± standard deviation. The single asterisk symbol (*) represents $p < 0.05$, the double asterisk symbol (**) represents $p < 0.01$ and the triple asterisk symbol (***) represents $p < 0.001$.

4. Experimental section

4.1. Synthesis of 2-(4-nitrophenyl)-1H-imidazo[4,5-f][1,10]-phenanthroline (PIP-NO_2)

Ligand PIP-NO_2 was synthesized with modifications according to the previously reported method [46]. 4-nitrobenzaldehyde (1.57 g, 10.39 mmol), 1,10-phenanthroline-5,6-dione (2.12 g, 10.08 mmol), and ammonium acetate (15.44 g, 200 mmol) were suspended in glacial acetic acid (80 mL). The resulting suspension was heated to reflux for 6 h. After completion of the reaction, the reaction mixture was adjusted to pH = 7 with concentrated aqueous ammonia. The resulting precipitate was collected by filtration, washed with water, and collected as a solid, which was then dried under the vacuum to get a bright yellow solid PIP-NO_2. Yield: 86% (2.93 g, 8.59 mmol). Anal. Calcd(%) for $C_{19}H_{11}N_5O_2$: C, 66.86; H, 3.25; N, 20.52. Found: C, 66.80; H, 3.28; N, 20.54. ESI-MS: $m/z = 342.09964$ ($[M+H]^+$). ^{1}H NMR (600 MHz, DMSO-d_6): $\delta = 9.05$ (dd, $J = 4.3$, 1.7 Hz, 2H), 8.93 (dd, $J = 8.1$, 1.8 Hz, 2H),

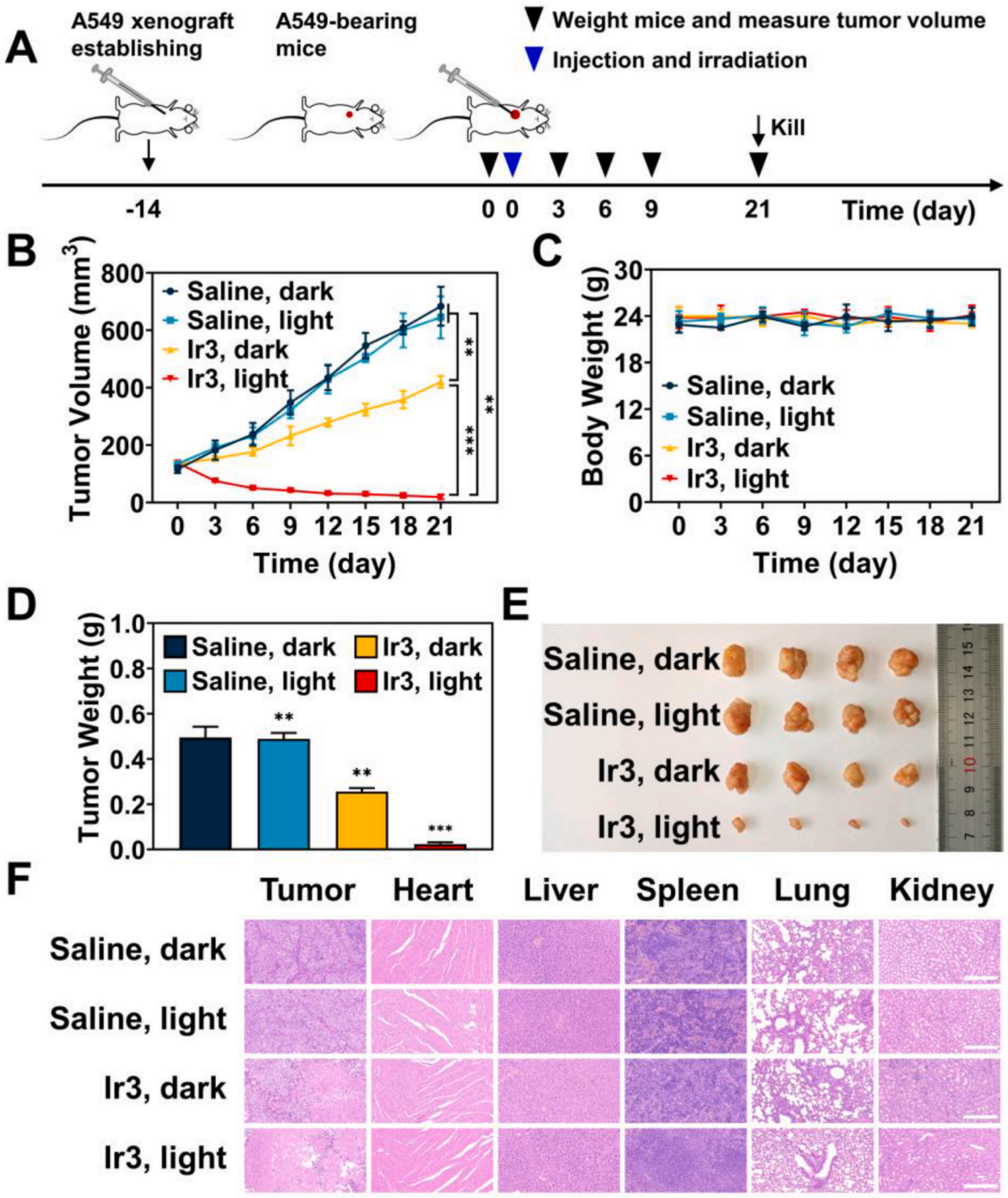

Fig. 10. Anti-proliferative activity of **Ir3** in A549 xenograft-bearing mice. (A) Scheme of anti-tumor experimentation. (B) The average tumor volume, (C) body weight and (D) the average tumor weight of nude mice in saline control (in the dark and under the light), **Ir3** (20 mg/kg, in the dark) and **Ir3** (20 mg/kg, under the light) groups. Each group consisted of five mice, and the data are presented as mean ± SD. The double asterisk symbol (**) represents $p < 0.01$ and the triple asterisk symbol (***) represents $p < 0.001$. (E) Photographs of tumors removed from A549 xenograft-bearing mice. (F) Histological hematoxylin and eosin (H&E) analysis of the tumor tissues and major organ tissues (heart, liver, spleen, lung, and kidney) collected from mice in the different groups at the end of treatment. Scale bars, 100 μm.

8.54 (d, $J = 8.9$ Hz, 2H), 8.48 (d, $J = 8.8$ Hz, 2H), 7.85 (dd, $J = 8.1$, 4.3 Hz, 2H).

4.2. Synthesis of 4-(1H-imidazo[4,5- f][1,10]phenanthroline-2-yl) aniline (PIP-NH_2)

Ligand PIP-NH_2 was synthesized with modifications according to the previously reported method [46]. 2-(4-nitrophenyl)-1H-imidazo[4,5-f][1,10]-phenanthroline (PIP-NO_2) (2.00 g, 5.86 mmol) was suspended in 1,4-dioxane (60 mL) and heated to 80 °C. $Na_2S{\cdot}9H_2O$ (4.22 g, 17.57 mmol) was dissolved in water (20 mL) and heated to 80 °C. The warm Na_2S solution was added to the yellow suspension, and the mixture was stirred at 80 °C for 4 h until the solid completely dissolved and the color of the solution changed from orange to red. The dioxane was evaporated, and the precipitate was collected and washed with water and ether respectively. The product PIP-NH_2 was dried under vacuum and

obtained as an ochre solid in a yield of 80% (1.44 g, 4.63 mmol). Anal. Calcd(%) for $C_{19}H_{13}N_5$: C, 73.30; H, 4.21; N, 22.49. Found: C, 73.28; H, 4.22; N, 22.51. ESI-MS: m/z = 312.12549 ($[M+H]^+$). ^{1}H NMR (600 MHz, DMSO- d_6): δ = 13.32 (s, 1H), 9.00 (dd, J = 4.3, 1.8 Hz, 2H), 8.89 (dd, J = 8.1, 1.8 Hz, 2H), 7.97 (d, J = 8.6 Hz, 2H), 7.81 (dd, J = 8.1, 4.3 Hz, 2H), 6.74 (d, J = 8.6 Hz, 2H), 5.63 (s, 2H).

4.3. Synthesis of N-(4-(1H-imidazo[4,5-f][1,10]phenanthrolin-2-yl) phenyl)-5-(2-oxohexahydro-1H-thieno [3,4-d]imidazole-4-yl)pentanam ide (PIP-Biotin)

4-(1H-imidazo[4,5-f][1,10]phenanthroline-2-yl)aniline (PIP-NH_2) (0.80 g, 2.56 mmol) and biotin (0.62 g, 2.56 mmol) were dissolved in anhydrous dichloromethane and cooled to 0 °C. Then, 1-Ethyl-3-(3′-dimethylaminopropyl)carbodiimide hydrochloride (EDCI) (1.23 g, 6.40 mmol) and 4-Dimethylaminopyridine (DMAP) (0.31 g, 2.56 mmol) were added to the mixture. The reaction mixture was stirred at 0 °C for 1 h and then slowly warmed to room temperature, and the reaction was allowed to continue for 12 h at room temperature. After the reaction was completed, the dichloromethane was removed and the residue was dissolved in water (50 mL), filtered and the precipitate collected. The precipitate was then dispersed in acetonitrile, filtered and the precipitate collected. After vacuum drying, a dark red PIP-Biotin product was obtained with a yield of 83% (1.14 g, 2.12 mmol). Anal. Calcd(%) for $C_{29}H_{27}N_7O_2S$: C, 64.79; H, 5.06; N, 18.24. Found: C, 64.75; H, 5.10; N, 18.25. ESI-MS: m/z = 538.20522 ($[M+H]^+$). ^{1}H NMR (600 MHz, DMSO- d_6): δ = 13.67 (s, 1H), 10.17 (s, 1H), 9.04 (dd, J = 4.2, 1.8 Hz, 2H), 8.93 (ddd, J = 11.3, 8.1, 1.8 Hz, 2H), 8.23 (d, J = 8.7 Hz, 2H), 7.91–7.77 (m, 4H), 6.44 (d, J = 47.3 Hz, 2H), 4.33 (dd, J = 7.7, 5.0 Hz, 1H), 4.16 (ddd, J = 7.5, 4.5, 1.8 Hz, 1H), 3.15 (ddd, J = 8.6, 6.1, 4.4 Hz, 1H), 2.84 (dd, J = 12.4, 5.1 Hz, 1H), 2.60 (d, J = 12.4 Hz, 1H), 2.38 (td, J = 7.2, 2.1 Hz, 2H), 1.71–1.36 (m, 6H).

4.3. Synthesis of 2-phenyl-1H-imidazo[4,5-f][1,10]phenanthroline (PIP)

The ligand PIP was synthesized according to the methods described previously [47].

4.4. Synthesis of Ir(III) dimer

The cyclometalated Ir(III) chloro-bridged dimers $[Ir(ppy)_2Cl]_2$ (Ir (III) dimer-1), $[Ir(dfppy)_2Cl]_2$ (Ir(III) dimer-2), and $[Ir(1\text{-}pq)_2Cl]_2$ (Ir(III) dimer-3) were synthesized according to the methods described previously [48–50].

4.5. Synthesis of Ir complexes

0.15 mmol of Ir-dimer (1 eq.) and 0.30 mmol of PIP-Biotin or PIP (2 eq.) were dissolved in a mixture of 21 mL 2:1 CH_2Cl_2/CH_3OH (v/v). The mixture was refluxed under an argon atmosphere for 24 h in the dark. After completion of the reaction, the mixture was cooled to room temperature and 6-fold excess NH_4PF_6 was added under vigorous stirring for 2 h to yield a precipitate. The precipitate was collected by filtration, washed with a small amount of ether, and dried under vacuum. The desired product was obtained by purifying the crude product through neutral Al_2O_3 column chromatography using a flow of CH_2Cl_2/CH_3OH (10:1, v/v).

$[Ir(ppy)_2(PIP\text{-}Biotin)]PF_6$ (**Ir1**) Yield：58% (0.205g, 0.173 mmol). Anal. Calcd(%) for $C_{51}H_{43}F_6IrN_9O_2PS$: C, 51.77; H, 3.66; N, 10.65. Found: C, 51.75; H, 3.63; N, 10.64. ESI-MS: m/z = 1038.28712 ($[M - PF_6]^+$). ^{1}H NMR (600 MHz, DMSO-d_6): δ = 14.30 (s, 1H), 10.18 (s, 1H), 9.18 (d, J = 8.3 Hz, 2H), 8.27 (d, J = 8.8 Hz, 4H), 8.13 (d, J = 4.9 Hz, 2H), 8.06 (dd, J = 8.3, 5.1 Hz, 2H), 7.96 (dd, J = 8.0, 1.4 Hz, 2H), 7.93–7.77 (m, 4H), 7.50 (dd, J = 5.9, 1.6 Hz, 2H), 7.07 (td, J = 7.6, 1.3 Hz, 2H), 7.04–6.87 (m, 4H), 6.45 (s, 1H), 6.38 (s, 1H), 6.30 (dd, J = 7.6, 1.2 Hz, 2H), 4.32 (dd, J = 7.8, 5.1 Hz, 1H), 4.16 (ddd, J = 7.4, 4.6, 1.9 Hz, 1H), 3.14 (ddd, J = 8.6, 6.1, 4.5 Hz, 1H), 2.84 (dd, J = 12.4, 5.1 Hz, 1H), 2.59 (d, J = 12.4 Hz, 1H), 2.38 (t, J = 7.1 Hz, 2H), 1.67 (dd, J = 14.6, 7.1 Hz, 3H), 1.55 (dd, J = 14.8, 6.0 Hz, 1H), 1.45–1.38 (m, 2H)

$[Ir(dfppy)_2(PIP\text{-}Biotin)]PF_6$ (**Ir2**) Yield：61% (0.229g, 0.183 mmol). Anal. Calcd(%) for $C_{51}H_{39}F_{10}IrN_9O_2PS$: C, 48.80; H, 3.13; N, 10.04. Found: C, 48.82; H, 3.10; N, 10.02. ESI-MS: m/z = 1110.24815 ($[M - PF_6]^+$). ^{1}H NMR (600 MHz, DMSO- d_6): δ = 14.28 (s, 1H), 10.20 (s, 1H), 9.21 (d, J = 8.3 Hz, 2H), 8.37–8.17 (m, 6H), 8.09 (s, 2H), 7.98 (t, J = 8.2 Hz, 2H), 7.86 (d, J = 8.3 Hz, 2H), 7.57 (d, J = 5.9 Hz, 2H), 7.13–6.98 (m, 4H), 6.42 (d, J = 45.2 Hz, 2H), 5.72 (dd, J = 8.3, 2.4 Hz, 2H), 4.32 (dd, J = 7.7, 5.2 Hz, 1H), 4.19–4.12 (m, 1H), 3.17–3.12 (m, 1H), 2.84 (dd, J = 12.4, 5.1 Hz, 1H), 2.59 (d, J = 12.4 Hz, 1H), 2.38 (t, J = 7.4 Hz, 2H), 1.66 (dd, J = 14.6, 7.1 Hz, 3H), 1.54 (dd, J = 14.8, 6.0 Hz, 1H), 1.44–1.37 (m, 2H). Elemental Analysis: C, 55.18; H, 3.54; N, 11.35; O, 2.88.

[Ir(1-pq)2(PIP-Biotin)]PF6 (Ir3) Yield：64% (0.246g, 0.192 mmol). Anal. Calcd(%) for C59H47F6IrN9O2PS: C, 55.22; H, 3.69; N, 9.82. Found: C, 55.24; H, 3.67; N, 9.83. ESI-MS: m/z = 1138.32283 ($[M - PF_6]^+$). ^{1}H NMR (600 MHz, DMSO- d_6): δ = 14.26 (s, 1H), 10.23 (d, J = 8.7 Hz, 1H), 9.19 (d, J = 8.3 Hz, 2H), 9.03 (d, J = 8.2 Hz, 2H), 8.42 (d, J = 8.1 Hz, 2H), 8.26 (d, J = 8.3 Hz, 2H), 8.13–7.99 (m, 6H), 7.88 (dd, J = 9.0, 4.3 Hz, 6H), 7.47–7.36 (m, 4H), 7.18 (q, J = 6.8, 6.0 Hz, 2H), 6.98 (t, J = 7.7 Hz, 2H), 6.46 (s, 1H), 6.39 (s, 1H), 6.30 (d, J = 7.6 Hz, 2H), 4.34–4.30 (m, 1H), 4.16 (dd, J = 7.5, 4.5 Hz, 1H), 3.14 (dt, J = 10.4, 5.0 Hz, 1H), 2.84 (dd, J = 12.4, 5.2 Hz, 1H), 2.58 (d, J = 12.4 Hz, 1H), 2.39 (t, J = 7.4 Hz, 2H), 1.66 (dd, J = 14.6, 7.1 Hz, 3H), 1.53 (dd, J = 14.8, 6.0 Hz, 1H), 1.46–1.37 (m, 2H).

$[Ir(1\text{-}pq)_2(PIP)]PF_6$ (**Ir3-NB**) Yield：56% (0.212g, 0.203 mmol). Anal. Calcd(%) for $C_{49}H_{32}F_6IrN_6P$: C, 56.48; H, 3.10; N, 8.07. Found: C, 56.24; H, 3.07; N, 8.11. ESI-MS: m/z = 897.22456 ($[M - PF_6]^+$). ^{1}H NMR (600 MHz, DMSO- d_6): δ = 9.15 (d, J = 8.2 Hz, 2H), 9.03 (d, J = 8.2 Hz, 2H), 8.38 (dd, J = 39.8, 7.9 Hz, 4H), 8.07–7.83 (m, 10H), 7.59 (t, J = 7.6 Hz, 2H), 7.53–7.38 (m, 5H), 7.18 (t, J = 7.7 Hz, 2H), 6.97 (t, J = 7.4 Hz, 2H), 6.32 (d, J = 7.6 Hz, 2H).

CRediT authorship contribution statement

Lai Wei: Conceptualization, Data curation, Investigation, Methodology, Writing – original draft. **Xiangdong He:** Methodology, Investigation, Validation. **Xinyue Shang:** Conceptualization, Methodology. **Martha Kandawa-Shultz:** Conceptualization, Methodology. **Guoqiang Shao:** Supervision, Resources. **Yihong Wang:** Resources, Supervision, Project administration, Writing – review & editing, All authors have approved the manuscript.

Declaration of competing interest

The authors declare that they have no known competing financial interests or personal relationships that could have appeared to influence the work reported in this paper.

Data availability

Data will be made available on request.

Acknowledgements

This work was supported by the National Natural Science Foundation of China (No. 81571812), A Project Funded by the Priority Academic Program Development of Jiangsu Higher Education Institutions (1107047002), Jiangsu Provincial Medical Youth Talent (QNRC2016075), The Nanjing Medical Science and Technique Development Foundation (ZKX19022) and Jiangsu Provincial High-level health talent “six one project” (LGY2019005).

Appendix A. Supplementary data

Supplementary data to this article can be found online at https://doi.org/10.1016/j.dyepig.2023.111641.

References

[1] Siegel RL, Miller KD, Wagle NS, Jemal A. Cancer statistics, 2023. CA A Cancer J Clin 2023;73(1):17–48.
[2] Guo X, Yang N, Ji W, Zhang H, Dong X, Zhou Z, et al. Mito-bomb: targeting mitochondria for cancer therapy. Adv Mater 2021;33(43):2007778.
[3] Wang Y, Huang X, Tang Y, Zou J, Wang P, Zhang Y, et al. A light-induced nitric oxide controllable release nano-platform based on diketopyrrolopyrrole derivatives for pH-responsive photodynamic/photothermal synergistic cancer therapy. Chem Sci 2018;9(42):8103–9.
[4] Li J, Wei K, Zuo S, Xu Y, Zha Z, Ke W, et al. Light-triggered clustered vesicles with self-supplied oxygen and tissue penetrability for photodynamic therapy against hypoxic tumor. Adv Funct Mater 2017;27(33):1702108.
[5] Deng Y, Pan S, Zheng J, Hong Y, Liu J, Chang H, et al. Electrostatic self-assembled Iridium(III) nano-photosensitizer for selectively disintegrated and mitochondria targeted photodynamic therapy. Dyes Pigments 2020;175:108105.
[6] Feng W-W, Liang B-F, Chen B-H, Liu Q-Y, Pan Z-Y, Liu Y-J, et al. A tricarbonyl rhenium(I) complex decorated with boron dipyrromethene for endoplasmic reticulum-targeted photodynamic therapy. Dyes Pigments 2023;211:111077.
[7] Liu S, Han J, Chang Y, Wang W, Wang R, Wang Z, et al. AIE-active iridium(III) complex integrated with upconversion nanoparticles for NIR-irradiated photodynamic therapy. Chem Commun 2022;58(72):10056–9.
[8] Yuan M, Fang X, Liu J, Yang K, Xiao S, Yang S, et al. NIR-II self-luminous molecular probe for in vivo inflammation tracking and cancer PDT effect self-evaluating. Small 2023;19(11):2206666.
[9] Gourdon L, Cariou K, Gasser G. Phototherapeutic anticancer strategies with first-row transition metal complexes: a critical review. Chem Soc Rev 2022;51(3):1167–95.
[10] Zamora A, Vigueras G, Rodríguez V, Santana MD, Ruiz J. Cyclometalated iridium (III) luminescent complexes in therapy and phototherapy. Coord Chem Rev 2018;360:34–76.
[11] Benson S, de Moliner F, Fernandez A, Kuru E, Asiimwe NL, Lee JS, et al. Photoactivatable metabolic warheads enable precise and safe ablation of target cells in vivo. Nat Commun 2021;12(1):2369.
[12] Gallardo-Villagran M, Leger DY, Liagre B, Therrien B. Photosensitizers used in the photodynamic therapy of rheumatoid arthritis. Int J Mol Sci 2019;20(13):3339.
[13] Miranda D, Carter K, Luo D, Shao S, Geng J, Li C, et al. Multifunctional liposomes for image-guided intratumoral chemo-phototherapy. Adv Healthcare Mater 2017;6(16):1700253.
[14] Xu H, Ohulchanskyy TY, Yakovliev A, Zinyuk R, Song J, Liu L, et al. Nanoliposomes Co-encapsulating CT imaging contrast agent and photosensitizer for enhanced, imaging guided photodynamic therapy of cancer. Theranostics 2019;9(5):1323–35.
[15] Qi S, Kwon N, Yim Y, Nguyen VN, Yoon J. Fine-tuning the electronic structure of heavy-atom-free BODIPY photosensitizers for fluorescence imaging and mitochondria-targeted photodynamic therapy. Chem Sci 2020;11(25):6479–84.
[16] Chen D, Zhao H, Shao T, Lu X, Fang Z, Cao H, et al. A cyclometallated iridium(III) complex with multi-photon absorption properties as an imaging-guided photosensitizer. J Mater Chem B 2022;10(30):5765–73.
[17] Kelland L. The resurgence of platinum-based cancer chemotherapy. Nat Rev Cancer 2007;7(8):573–84.
[18] He L, Li Y, Tan CP, Ye RR, Chen MH, Cao JJ, et al. Cyclometalated iridium(iii) complexes as lysosome-targeted photodynamic anticancer and real-time tracking agents. Chem Sci 2015;6(10):5409–18.
[19] Wang X, Song K, Deng Y, Liu J, Peng Q, Lao X, et al. Benzothiazole-decorated iridium-based nanophotosensitizers for photodynamic therapy of cancer cells. Dalton Trans 2022;51(9):3666–75.
[20] Li X, Wu J, Wang L, He C, Chen L, Jiao Y, et al. Mitochondrial-DNA-targeted Ir(III)-containing metallohelices with tunable photodynamic therapy efficacy in cancer cells. Angew Chem Int Ed Engl 2020;59(16):6420–7.
[21] Kuang S, Wei F, Karges J, Ke L, Xiong K, Liao X, et al. Photodecaging of a mitochondria-localized iridium(III) endoperoxide complex for two-photon photoactivated therapy under hypoxia. J Am Chem Soc 2022;144(9):4091–101.
[22] Li J, Guo L, Tian Z, Zhang S, Xu Z, Han Y, et al. Half-sandwich iridium and ruthenium complexes: effective tracking in cells and anticancer studies. Inorg Chem 2018;57(21):13552–63.
[23] Ma W, Ge X, Guo L, Zhang S, Li J, He X, et al. Bichromophoric anticancer drug: targeting lysosome with rhodamine modified cyclometalated Iridium(III) complexes. Dyes Pigments 2019;162:385–93.
[24] Zhang DY, Zheng Y, Zhang H, Sun JH, Tan CP, He L, et al. Delivery of phosphorescent anticancer iridium(III) complexes by polydopamine nanoparticles for targeted combined photothermal-chemotherapy and thermal/photoacoustic/lifetime imaging. Adv Sci 2018;5(10):1800581.
[25] Manna S, Kakumachi S, Das KK, Tsuchiya Y, Adachi C, Panda S. Mechanistic dichotomy in the solvent dependent access to E vs. Z-allylic amines via decarboxylative vinylation of amino acids. Chem Sci 2022;13(33):9678–84.
[26] Yang X, Zhou X, Zhang YX, Li D, Li C, You C, et al. Blue phosphorescence and hyperluminescence generated from imidazo[4,5-b]pyridin-2-ylidene-based iridium (III) phosphors. Adv Sci 2022;9(25):2201150.
[27] Wang L, Monro S, Cui P, Yin H, Liu B, Cameron CG, et al. Heteroleptic Ir(III)N(6) complexes with long-lived triplet excited states and in vitro photobiological activities. ACS Appl Mater Interfaces 2019;11(4):3629–44.
[28] Moura NMM, Castro KADF, Biazzotto JC, Prandini JA, Lodeiro C, Faustino MAF, et al. Ruthenium and iridium complexes bearing porphyrin moieties: PDT efficacy against resistant melanoma cells. Dyes Pigments 2022;205:110501.
[29] Zhong M, He J, Zhang B, Liu Q, Fang J. Mitochondria-targeted iridium-based photosensitizers enhancing photodynamic therapy effect by disturbing cellular redox balance. Free Radic Biol Med 2023;195:121–31.
[30] Aoki S, Yokoi K, Hisamatsu Y, Balachandran C, Tamura Y, Tanaka T. Post-complexation functionalization of cyclometalated iridium(III) complexes and applications to biomedical and material sciences. Top Curr Chem 2022;380(5):36.
[31] Sato K, Nagaya T, Mitsunaga M, Choyke PL, Kobayashi H. Near infrared photoimmunotherapy for lung metastases. Cancer Lett 2015;365(1):112–21.
[32] Abou-El-Naga AM, Mutawa G, El-Sherbiny IM, Mousa SA. Activation of polymeric nanoparticle intracellular targeting overcomes chemodrug resistance in human primary patient breast cancer cells. Int J Nanomed 2018;13:8153–64.
[33] Fam KT, Collot M, Klymchenko AS. Probing biotin receptors in cancer cells with rationally designed fluorogenic squaraine dimers. Chem Sci 2020;11(31):8240–8.
[34] Wang K, Liu Y, Liu C, Zhu H, Li X, Yu M, et al. A new-type HOCl-activatable fluorescent probe and its applications in water environment and biosystems. Sci Total Environ 2022;839:156164.
[35] Ren WX, Han J, Uhm S, Jang YJ, Kang C, Kim JH, et al. Recent development of biotin conjugation in biological imaging, sensing, and target delivery. Chem Commun 2015;51(52):10403–18.
[36] Maiti S, Paira P. Biotin conjugated organic molecules and proteins for cancer therapy: a review. Eur J Med Chem 2018;145:206–23.
[37] Liu L, Liu F, Liu D, Yuan W, Zhang M, Wei P, et al. A smart theranostic prodrug system activated by reactive oxygen species for regional chemotherapy of metastatic cancer. Angew Chem Int Ed Engl 2022;61(12):202116807.
[38] Abdul Pari AA, Singhal M, Hubers C, Mogler C, Schieb B, Gampp A, et al. Tumor cell-derived angiopoietin-2 promotes metastasis in melanoma. Cancer Res 2020;80(12):2586–98.
[39] Deng W, McKelvey KJ, Guller A, Fayzullin A, Campbell JM, Clement S, et al. Application of mitochondrially targeted nanoconstructs to neoadjuvant X-ray-induced photodynamic therapy for rectal cancer. ACS Cent Sci 2020;6(5):715–26.
[40] Mari C, Pierroz V, Ferrari S, Gasser G. Combination of Ru(ii) complexes and light: new frontiers in cancer therapy. Chem Sci 2015;6(5):2660–86.
[41] Zhao X, Zhao KC, Chen LJ, Liu YS, Liu JL, Yan XP. A pH reversibly activatable NIR photothermal/photodynamic-in-one agent integrated with renewable nanoimplants for image-guided precision phototherapy. Chem Sci 2020;12(1):442–52.
[42] Riethmuller M, Burger N, Bauer G. Singlet oxygen treatment of tumor cells triggers extracellular singlet oxygen generation, catalase inactivation and reactivation of intercellular apoptosis-inducing signaling. Redox Biol 2015;6:157–68.
[43] Cortes CJ, Miranda HC, Frankowski H, Batlevi Y, Young JE, Le A, et al. Polyglutamine-expanded androgen receptor interferes with TFEB to elicit autophagy defects in SBMA. Nat Neurosci 2014;17(9):1180–9.
[44] Li N, Yu L, Wang J, Gao X, Chen Y, Pan W, et al. A mitochondria-targeted nanoradiosensitizer activating reactive oxygen species burst for enhanced radiation therapy. Chem Sci 2018;9(12):3159–64.
[45] Gao N, Zhang Q, Mu Q, Bai Y, Li L, Zhou H, et al. Steering carbon nanotubes to scavenger receptor recognition by nanotube surface chemistry modification partially alleviates NFkappaB activation and reduces its immunotoxicity. ACS Nano 2011;5(6):4581–91.
[46] Shi H, Lou J, Lin S, Wang Y, Hu Y, Zhang P, et al. Diatom-like silica-protein nanocomposites for sustained drug delivery of ruthenium polypyridyl complexes. J Inorg Biochem 2021;221:111489.
[47] Szlapa-Kula A, Palion-Gazda J, Ledwon P, Erfurt K, Machura B. A fundamental role of the solvent polarity and remote substitution of the 2-(4-R-phenyl)-1H-imidazo[4,5-f][1,10]phenanthroline framework in controlling the ground- and excited-state properties of Re(I) chromophores [ReCl(CO)(3)(R-C(6)H(4)-imphen)]. Dalton Trans 2022;51(38):14466–81.
[48] Ru JX, Guan LP, Tang XL, Dou W, Yao X, Chen WM, et al. Turn-on phosphorescent chemodosimeter for Hg2+ based on a cyclometalated Ir(III) complex and its application in time-resolved luminescence assays and live cell imaging. Inorg Chem 2014;53(21):11498–506.
[49] Baranoff E, Curchod BF, Monti F, Steimer F, Accorsi G, Tavernelli I, et al. Influence of halogen atoms on a homologous series of bis-cyclometalated iridium(III) complexes. Inorg Chem 2012;51(2):799–811.
[50] Lepeltier M, Dumur F, Marrot J, Contal E, Bertin D, Gigmes D, et al. Unprecedented combination of regioselective hydrodefluorination and ligand exchange reaction during the syntheses of tris-cyclometalated iridium(III) complexes. Dalton Trans 2013;42(13):4479–86.